Journal of Solid State Chemistry 198 (2013) 386–391

Contents lists available at SciVerse ScienceDirect

Journal of Solid State Chemistry

journal homepage: www.elsevier.com/locate/jssc

$Cu_2Mn_{1-x}Co_xSnS_4$: Novel këserite type solid solutions

F. López-Vergara [a,*], A. Galdámez [a,*], V. Manríquez [a], P. Barahona [b], O. Peña [c]

[a] Departamento de Química, Facultad de Ciencias, Universidad de Chile, Santiago, Chile
[b] Facultad de Ciencias Básicas, Universidad Católica del Maule, Talca, Chile
[c] Institut des Sciences Chimiques de Rennes, UMR 6226, Université de Rennes 1, Rennes, France

ARTICLE INFO

Article history:
Received 23 August 2012
Received in revised form
25 October 2012
Accepted 26 October 2012
Available online 15 November 2012

Keywords:
Chalcogenide
Synthesis
Crystal structure
Këserite

ABSTRACT

A new family of $Cu_2Mn_{1-x}Co_xSnS_4$ chalcogenides has been synthesized by conventional solid-state reactions at 850 °C. The reactions products were characterized by powder X-ray diffraction (XRD), energy-dispersive X-ray analysis (SEM-EDS), Raman spectroscopy and magnetic susceptibility. The crystal structures of two members of the solid solution series $Cu_2Mn_{0.4}Co_{0.6}SnS_4$ and $Cu_2Mn_{0.2}Co_{0.8}SnS_4$ have been determined by single-crystal X-ray diffraction. Both phases crystallize in the tetragonal këserite-type structure (space group $I\bar{4}$). The distortions of the tetrahedral volume of $Cu_2Mn_{0.4}Co_{0.6}SnS_4$ and $Cu_2Mn_{0.2}Co_{0.8}SnS_4$ were calculated and compared with the corresponding differences in the Cu_2MnSnS_4 (stannite-type) end-member. The compounds show nearly the same Raman spectral features. Temperature-dependent magnetization measurements (ZFC/FC) and high-temperature susceptibility indicate that these solid solutions are antiferromagnetic.

1. Introduction

The compounds known as "adamantine" have a crystal structure similar to the structure of diamond, which is based on the different arrangement of cations and anions, and that satisfy the rule of four valence electrons average by atom [1,2]. In recent years, the adamantine compounds have attracted considerable attention for the development of photovoltaic materials as new sources of energy. The most common binary derivatives are based on the II–VI elements (II=Zn, Cd, Hg; VI=S, Se, Te) and have zinc blende-type structure [3,4]. In the case of ternary compounds, the most representative materials are AMQ_3 (I–III–VI_2 where A=Cu, Ag; M=Al, Ga, In and Q=S, Se, Te). In these derivatives, the c-axis of the cubic unit cell is doubled and they crystallize in a tetragonal chalcopyrite-type structure (the mineral $CuFeS_2$) [5]. The ternary I–III–VI_2 chalcopyrites have been used as absorbent layer in thin films for solar cells [6–9]. Other examples are related to quaternary compounds Cu_2ZnSnS_4 (CZTS), $Cu_2ZnSnSe_4$ and their solid solutions [10,11].

A symmetry reduction occurs in the quaternary compounds Cu_2MSnQ_4 (I_2–II–IV–VI_4) and they crystallize in structures of stannite-type (Cu_2FeSnS_4) and këserite-type (Cu_2ZnSnS_4) [12–16]. Both Cu_2MnSnS_4 and Cu_2CoSnS_4 end members of the solid solutions $Cu_2Mn_{1-x}Co_xSnS_4$ crystallizes in the space group $I\bar{4}2m$ (no. 121), which corresponds to the stannite-type structure [17,18]. The reduction of symmetry in this type of structure is characterized by an increase in the degree of freedom in the positions of the sulfide anion, going from the ideal (1/4,1/4,1/4) position in the Zinc blende to the (x,y,z) position in the këserite type structure:

Zinc blende (1/4, 1/4, 1/4)→chalcopyrite (x, 1/4, 1/8)→stannite (x, x, z)→këserite (x, y, z)

Another structural feature of this type of phases is the distribution of cations in the tetrahedral sites: Zn and Cu atoms in 2a, 2c and 2d sites for $I\bar{4}$ (këserite) and 2a (Fe atoms), 4d (Cu atoms) for $I\bar{4}2m$ (stannite). The tetrahedral site of Sn in both structures type is 2b. Bonazzi et al. [14] have performed a structural study of $Cu_2Fe_{1-x}Zn_xSnS_4$ showing that there are two mechanisms of incorporation of Cu^+, Fe^{2+} and Zn^{2+} cation metals in the tetrahedral cavities along the intermixing stannite–këserite series [10,11]. Recently, Schorr et al. conducted structure refinement on $Cu_2Fe_{1-x}Zn_xSnS_4$ solid solutions using neutron diffraction [15]. They reported the existence of one crossover from stannite to këserite when Fe^{2+} is substituted by Zn^{2+} (from x=1 to 0). The present work reports the results of the synthesis and characterization of the solid solution $Cu_2Mn_{1-x}Co_xSnS_4$. The aim of this work is to study the influence of the substitution of Co^{2+} by the paramagnetic Mn^{2+} cation on the crystal structure and magnetic properties of the solid solutions.

2. Experimental sections

2.1. Synthesis

The polycrystalline $Cu_2Mn_{1-x}Co_xSnS_4$ compounds were prepared by direct combination of powders of the corresponding

* Corresponding authors. Fax: +56 2 271 3888.
E-mail addresses: fer_martina@u.uchile.cl (F. López-Vergara), agaldamez@uchile.cl (A. Galdámez).

0022-4596/$ - see front matter © 2012 Published by Elsevier Inc.
http://dx.doi.org/10.1016/j.jssc.2012.10.026

high purity elements (99.99%, Aldrich) in stoichiometric amounts. All manipulations were carried out under Argon atmosphere. The reaction mixture was sealed in evacuated quartz ampoules, placed in a programmable furnace, heated to 850 °C for about 72 h, and then cooled by quenching in liquid nitrogen. The products appeared to be air- and moisture-stable over several weeks.

2.2. Structure determination

Two single crystals were selected from the $x=0.6$ and 0.8 reaction products. X-ray energy-dispersive spectroscopy (EDS) analysis (in several areas) showed the presence of Cu/Mn/Co/Sn/S in average molar ratios of 1.90:0.36:0.64:1.0:3.9 and 1.9:0.18:0.82:1.1:3.9, which are in reasonable agreement with the chemical compositions from their polycrystalline compounds. Single-crystal X-ray diffraction data of $Cu_2Mn_{0.4}Co_{0.6}SnS_4$ were collected at room temperature on a Bruker Kappa CCD diffractometer, using the graphite-monochromatized Mo$K\alpha_1$ radiation ($\lambda=0.71073$ Å). The collection of intensity data was carried out with the program COLLECT [19]. Cell refinement and data reduction were carried out with Dirax/lsq and EvalCCD programs [20,21]. Single-crystal X-ray diffraction data of $Cu_2Mn_{0.2}Co_{0.8}SnS_4$ were collected at room temperature on a APEXII Bruker-AXS, using the graphite-monochromatized Mo$K\alpha_1$ radiation ($\lambda=0.71073$ Å). The collection of intensity data was carried out with the program SMART [22]. Cell refinement and data reduction were carried out with the program SAINT [22]. Multi-scan absorption correction was performed with SADABS program [23]. The crystal structures of $Cu_2Mn_{0.4}Co_{0.6}SnS_4$ and $Cu_2Mn_{0.2}Co_{0.8}SnS_4$ were refined in full-matrix least-squares using the SHELXL package of crystallographic programs [24]. Molecular graphics: *DIAMOND* [25]; software used to prepare material for publication: *PLATON* [26]. The refined occupation factors of Mn and Co cations were consistent with the EDS chemical analysis averaged over several areas of the single crystals used for the diffraction experiment. Moreover, Mn and Co atoms (same crystallographic site) were constrained to have identical thermal parameters. Anisotropic thermal parameter refinements were applied to all atoms. Detailed crystallographic data and refinement results for $Cu_2Mn_{0.4}Co_{0.6}SnS_4$ and $Cu_2Mn_{0.2}Co_{0.8}SnS_4$ are summarized in Table 1. The atomic coordinates, equivalent isotropic thermal parameters, selected bond distances and angles are listed in Tables 2 and 3. Additional details can be found in the Supporting Information.

Table 1
Crystallographic data and structure refinement details for $Cu_2Mn_{1-x}Co_xSnS_4$.

Compound	$Cu_2Mn_{0.4}Co_{0.6}SnS_4$	$Cu_2Mn_{0.2}Co_{0.8}SnS_4$
Crystal size (mm^3)	$0.1\times0.08\times0.09$	$0.10\times0.07\times0.08$
Crystal color	Black	Black
Crystal system	Tetragonal	Tetragonal
Space group, Z	$I\bar{4}$ (no. 82), 2	$I\bar{4}$ (no. 82), 2
Lattice constants (Å)	$a=5.4288(8)$ $c=10.911(2)$	$a=5.4115(8)$ $c=10.847(2)$
Cell volume ($Å^3$)	321.56(9)	317.65(9)
Temperature (K)	293(2)	293(2)
Wavelength, Mo$K\alpha$	0.71073	0.71073
Equipment	Kappa CCD	APEXII, Bruker-AXS
Absorption coefficient (mm^{-1})	15.940	13.923
$F(000)$	448	396
θ-range (deg.)	$5.31<\theta<39.95$	$4.21<\theta<40.35$
hkl-range	$-9\le h\le9$ $-9\le k\le9$ $-18\le l\le19$	$-8\le h\le9$ $-9\le k\le9$ $-17\le l\le19$
No. of reflections, $R_{int.}$, R_σ	3555, 0.0277, 0.0294	6928, 0.0397, 0.0248
No. of independent reflections	981	994
No. of parameters	19	19
Extinction coefficient	0.0084(6)	0.0277(14)
R ($I>2\sigma_I$), R (all reflections)	0.0308, 0.0268	0.0196, 0.0196
wR_2 ($I>2\sigma_I$), wR_2 (all reflections)	0.0538, 0.0521	0.0483, 0.0483
Goodness-of-Fit (GooF=S)	1.125	1.120
Flack parameter	0.000	0.000
Largest difference peaks	0.713, −1.258	1.366, −0.449

Table 3
Selected bond distances (Å) and angles (deg.) for $Cu_2Mn_{1-x}Co_xSnS_4$ compounds with estimated standard deviations in parentheses.

Distances (Å)		Angles (deg.)	
$Cu_2Mn_{0.4}Co_{0.6}SnS_4$			
Cu1–S	$2.3451(11)\times4$	S^i–Sn–S^{ii}	109.34 (3)
Cu2–S	$2.3341(5)\times4$	S^i–Sn–S^{iii}	109.538 (13)
M^a–S	$2.3302(11)\times4$	S^{ii}–Sn–S^{iii}	109.538 (13)
Sn–S	$2.4107(5)\times4$	S^i–Sn–S	109.538 (13)
S–Cu1–S	$108.87(2)\times4$, $110.68(4)\times2$	S^{ii}–Sn–S	109.538 (13)
S–Cu2–S	$110.898(14)\times4$, $106.65(3)\times2$	S^{iii}–Sn–S	109.34 (3)
S–M^a–S	$109.12(2)\times4$, $110.18(4)\times2$	M^a—S—Sn	108.51 (4)
$Cu_2Mn_{0.2}Co_{0.8}SnS_4$			
Cu1–S	$2.3296(10)\times4$	S^i–Sn–S^{ii}	109.22 (2)
Cu2–S	$2.3261(4)\times4$	S^i–Sn–S^{iii}	109.595 (10)
M^a–S	$2.3144(10)\times4$	S^{ii}–Sn–S^{iii}	109.595 (10)
Sn–S	$2.4126(5)\times4$	S^i–Sn–S	109.595 (10)
S–Cu1–S	$108.569(17)\times2$, $111.29(4)\times4$	S^{ii}–Sn–S	109.595 (10)
S–Cu2–S	$106.17(2)\times2$, $111.148(11)\times4$	S^{iii}–Sn–S	109.22 (2)
S–M^a–S	$108.823(18)\times4$, $110.78(4)\times2$	M^a–S–Sn	108.25 (4)

[a] M represents the 2d positions statistically occupied by Mn and Co Symmetry code: (i) $-1+y$, $1-x$, $1-z$; (ii) $1-y$, $1+x$, $1-z$; (iii) $-x$, $2-y$, z.

Table 2
Atomic coordinates and equivalent isotropic displacement parameters ($Å^2$) for $Cu_2Mn_{1-x}Co_xSnS_4$.

Atom	Wyckoff multiplicity	Occupancy	x	y	z	U_{eq}[a]
$Cu_2Mn_{0.4}Co_{0.6}SnS_4$						
Cu1	2c	1	1/2	1	3/4	0.0153 (7)
Cu2	2a	1	1/3	1/2	1/2	0.01971 (17)
Mn/Co	2d	0.4/0.6	0	1/2	3/4	0.0186 (8)
Sn	2b	1	0	1	1/2	0.01241 (8)
S	8g	1	0.2550 (2)	0.74264 (15)	0.62778 (4)	0.01288 (10)
$Cu_2Mn_{0.2}Co_{0.8}SnS_4$						
Cu1	2c	1	1/2	1	3/4	0.0130 (4)
Cu2	2a	1	1/2	1/2	1/2	0.01774 (12)
Mn/Co	2d	0.2/0.8	0	1/2	3/4	0.0173 (5)
Sn	2b	1	0	1	1/2	0.01057 (5)
S	8g	1	0.25579 (17)	0.74180 (13)	0.62880 (3)	0.01132(9)

[a] U_{eq} is defined as one-third of the trace of the orthogonalized U_{ij} tensor.

2.3. Powder X-ray diffraction measurements

Powder X-ray diffraction patterns were collected, at room temperature, on Siemens D5000 powder diffractometer, with Cu$K\alpha$ radiation (λ=1.541871 Å) in the range $5^\circ < 2\theta < 80^\circ$. The XRD patterns were indexed with the computer program CHECK-CELL [27].

2.4. SEM-EDS analysis

The chemical compositions of the samples were determined by scanning electron microscopy with the aid of energy-dispersive X-ray analysis (SEM-EDS) using a JEOL 5400 system equipped with an Oxford LinK ISIS microanalyzer. The working distance was 35 mm and the accelerating voltage was set to 22.5 kV. Samples were mounted onto double-sided carbon tape, which was adhered to an aluminum specimen holder. EDS data were collected for 60 s.

2.5. Raman spectroscopy

The Raman spectra in selected crystals and powder samples were recorded in the frequency range between 150 and 3500 cm^{-1} using a micro-Raman Renishaw system 1000 equipped with Leica-DMLM microscope. The spectra data were collected at room temperature with laser line of 633 nm and laser power of 1 mW. The spectra of the samples are uniform throughout the scanned region of single crystals.

2.6. Magnetic measurement

Magnetic measurements were performed on pelletized powder samples using a Quantum Design MPMS XL5 SQUID magnetometer between 2 and 400 K, under different applied fields (500 Oe for zero-field-cooled/field-cooled (ZFC/FC) cycles and 10 kOe for high-temperature susceptibility measurements).

3. Results and discussion

3.1. Crystal structure

The Cu_2MnSnS_4 end member of the solid solutions $Cu_2Mn_{1-x}Co_xSnS_4$ crystallizes in the space group $I\bar{4}2m$ (no. 121), which corresponds to the stannite-type structure. Thus, at the beginning, the phases $Cu_2Mn_{0.4}Co_{0.6}SnS_4$ and $Cu_2Mn_{0.2}Co_{0.8}SnS_4$ were refined in this space group, where the Cu atoms are located in the 4*d* position (Co, Mn), in 2*a*, Sn at 2*b* and S atoms at 8*i*. However, a careful examination of the structural details, such as the Flack parameter and the thermal equivalent isotropic displacement (U_{eq}), the R and wR_2 statistical parameters gave a strong indication of inconsistency. On the other hand, Schorr et al. carried out a neutron diffraction study of the solid solutions $Cu_2Fe_{1-x}Zn_xSnS_4$, obtaining that the $c/2a$-ratio of the lattice constants has a value equal to or greater than 1.000 for kësterite-type structures (space group $I\bar{4}$) [15]. The $c/2a$-ratios for the phases $Cu_2Mn_{0.4}Co_{0.6}SnS_4$ and $Cu_2Mn_{0.2}Co_{0.8}SnS_4$ are 1.0049 and 1.0022, respectively. For these reasons, the refinement of the structure was repeated in the kësterite space group $I\bar{4}$ (no. 82). Different structural models were refined for the permutations of the metal atoms positions. These models were based on different distributions of Co, Mn and Cu atoms in 2*a*, 2*c* and 2*d* for $I\bar{4}$ and 2*a*, 4*d* for $I\bar{4}2m$. Owing to the different atoms distributions in 2*c* and 2*d*, the mirror plane parallel to (110) in $I\bar{4}2m$ group space (stannite structure) is lost in $I\bar{4}$ space group (kësterite structure). The model with space group $I\bar{4}$ and occupation sites 2*a*=Cu2, 2*c*=(1−*x*)Mn+*x*Co and 2*d*=Cu1, with two different crystallographic Cu^+ cations gave better refinement results (see Table 1).

The $Cu_2Mn_{0.4}Co_{0.6}SnS_4$ and $Cu_2Mn_{0.2}Co_{0.8}SnS_4$ phases are isostructural and adopt the three-dimensional kësterite structure-type (Fig. 1). The main features in the crystal structure are the tetrahedra MS_4 (M=Mn, Co, Cu and Sn). These structural tetrahedral motifs have been observed in other sulfides such as Cu_2ZnSnS_4 [14], Cu_2FeSnS_4 [14], Cu_2MnSnS_4 [17], and $Cu_2MnGe_{0.55}Sn_{0.45}S_4$ [28]. Since there are no S–S bonds in the structures, the oxidation states of Cu, (Mn/Co), Sn, and S can be assigned to 1+, 2+, 4+ and 2−, respectively. In both, $Cu_2Mn_{0.4}Co_{0.6}SnS_4$ and $Cu_2Mn_{0.2}Co_{0.8}SnS_4$ compounds, the distance and angles of the MS_4 tetrahedrons compare well with those found in kësterite series $Cu_2Fe_{1-x}Zn_xSnS_4$ [13,14], $Cu_2MnGe_{0.55}Sn_{0.45}S_4$, Cu_2MnSnS_4 and Cu_2CoGeS_4 [18,29].

Fig. 2 presents a polyhedral view of the crystal structure. There are five types of atoms-centered tetrahedra MS_4 ($Cu1S_4$, $Cu2S_4$, MS_4 and SnS_4) and moreover, each sulfur atoms is surrounded by four metal atoms. All polyhedra are oriented in the same direction and are connected by the corners (Fig. 2). One way to measure the

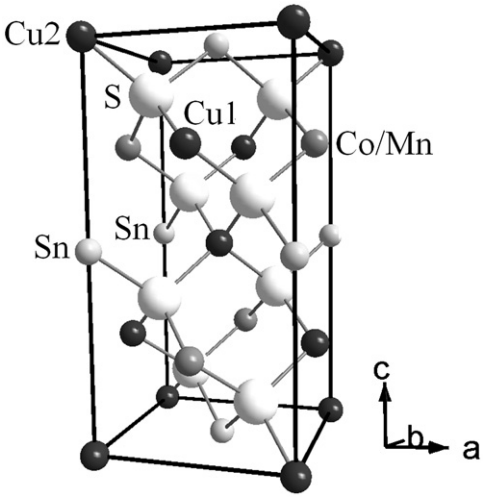

Fig. 1. Unit cell of the $Cu_2Mn_{1-x}Co_xSnS_4$ structure type viewed along [010].

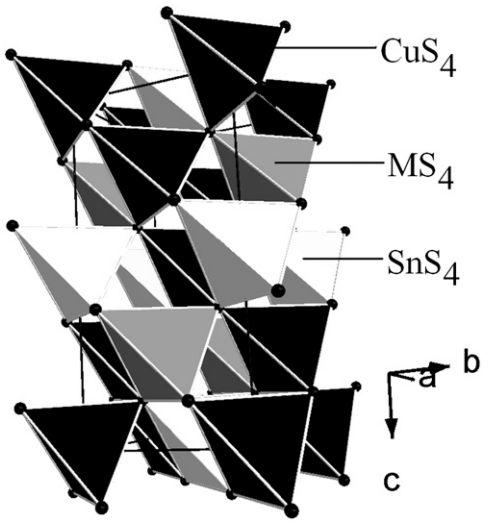

Fig. 2. View along [100] of the $Cu_2Mn_{1-x}Co_xSnS_4$ structure showing tetrahedral units. The figure shows polyhedra of [SnS_4], [CuS_4], [MS_4] (M=Mn, Co) with Sulfur atoms in the corners.

distortion of the tetrahedra is with the parameters of edge length distortion (ELD) and tetrahedral angle variance (TAV) [30]. The ELD parameter measures the distortion percentage of the edges of the tetrahedra from sulfur–sulfur bond distances. All the tetrahedra show a distortion less than 2%, which indicates near-ideal tetrahedra (Table 4). The *ELD* and *TAV* parameters show that the more distorted tetrahedra are the $Cu2S_4$ in both compounds, the distortion increases with the Co content, since Co^{2+} has a smaller ionic radius than Mn^{2+} in a tetrahedral coordination [31]. The SnS_4 tetrahedra, which are in the middle of the cell, are less distorted (see Fig. 1).

Arno Pfitzner et al. have presented a quantitative concept to investigate the distortions of the tetrahedral [17,28,29,32]. The $\overline{\Delta V_i}$-values are used to quantify the distortion of the tetrahedral in the crystalline structure and are used to separate the compounds with sphalerite-type superstructures from compounds with structure wurtzite-type superstructures. The tetrahedral volumes V_i can be calculated from the sulfur–sulfur distances (edge of tetrahedra). The V_i-values for $Cu_2Mn_{0.4}Co_{0.6}SnS_4$ and $Cu_2Mn_{0.2}Co_{0.8}SnS_4$ are reported in Table 4. The $\overline{V}$-values are calculated by following expression:

$$\overline{V} = \frac{\sum_i^n Wy_i V_i}{\sum_i^n Wy_i} \quad (1)$$

Table 4
Edge length distortion (*ELD*), tetrahedral angle variance (*TAV*) and tetrahedral volumes of $Cu_2Mn_{0.4}Co_{0.6}SnS_4$ and $Cu_2Mn_{0.2}Co_{0.8}SnS_4$.

Tetrahedral	*ELD*[a] (%)	*TAV*[b] (deg.)	Volume (Å^3)
$Cu_2Mn_{0.4}Co_{0.6}SnS_4$			
$Cu1S_4$	0.73	0.88	6.616
$Cu2S_4$	1.18	4.84	6.514
MS_4	0.29	0.31	6.493
SnS_4	0.05	0.01	7.191
$Cu_2Mn_{0.2}Co_{0.8}SnS_4$			
$Cu1S_4$	0.74	1.97	6.484
$Cu2S_4$	1.39	6.60	6.443
MS_4	0.53	1.01	6.360
SnS_4	0.10	0.04	7.206

[a] $EDL = (100/6)\sum_{l=1}^{6}(((S{-}S)_i - \langle S{-}S\rangle))/\langle S{-}S\rangle)\%$
[b] $TAV = \sum_{l=1}^{6}\left((\theta_i - 109.4712)^2/5\right)$
where θ_i are the angles of the S–Metal–S bonds in the tetrahedra and $\langle S{-}S\rangle$ is the average sulfur–sulfur distance in the tetrahedral edge.

Table 5
$\%\Delta V_i$ and $\%\overline{\Delta V_i}$-values of $Cu_2Mn_{0.2}Co_{0.8}SnS_4$, $Cu_2Mn_{0.4}Co_{0.6}SnS_4$ and Cu_2MnSnS_4 (stannite-type).

Compounds	$\%\Delta V_i$ **Cu(1)S$_4$**	$\%\Delta V_i$ **Cu(2)S$_4$**	$\%\Delta V_i$ ***M*S$_4$**	$\%\Delta V_i$ **SnS$_4$**	$\%\overline{\Delta V_i}$
$Cu_2Mn_{0.2}Co_{0.8}SnS_4$	−2.11	−2.67	−3.99	8.77	4.4
$Cu_2Mn_{0.4}Co_{0.6}SnS_4$	−1.30	−2.78	−3.15	7.23	3.6
Cu_2MnSnS_4[a]	−5.90	–	7.80	4.10	6.0

[a] Ref. [28].

where *Wy* is the Wyckoff number of cation's position in the unit cell. The ΔV_i and $\overline{\Delta V_i}$ values are calculated by following expressions:

$$\%\Delta V_i = \frac{V_i - \overline{V}}{\overline{V}} \times 100 \quad (2)$$

$$\%\overline{\Delta V_i} = \frac{\sum_i^n Wy_i |\Delta V_i|}{\sum_i^n Wy_i} \times 100 \quad (3)$$

The corresponding $\%\overline{\Delta V_i}$-values for the phase Cu_2MnSnS_4 is 6.0% while the $\%\overline{\Delta V_i}$-values in Cu_2MnSiS_4 (11.1%) indicate that these phases crystallize in stannite- and wurtzite-type structures, respectively [17]. The $\%\overline{\Delta V_i}$-values of both phases, reported herein, were calculated with (3). The $\%\overline{\Delta V_i}$ of $Cu_2Mn_{0.2}Co_{0.8}SnS_4$ and $Cu_2Mn_{0.4}Co_{0.6}SnS_4$ are 4.4% and 3.6%, respectively (see Table 5) and are smaller than the $\%\overline{\Delta V_i}$ of Cu_2MnSnS_4, consistent with a kësterite-type structure.

3.2. X-ray powder diffraction, spectroscopic and compositional characterization

The quantitative contents of the constituent elements were examined by energy dispersive SEM-EDS X-ray analysis in pelletized materials, over many grains and micro-crystals. It was found that the average concentrations of Mn, Co, Sn, Cu and S elements were close to the nominal compositions (Table 6). The X-ray powder patterns (XRD) showed sharp lines that reflect the crystallinity and homogeneity. Representative diffraction profiles are shown in Fig. 3. The experimental XRD powder patterns of the solid solutions were compared with simulated XRD patterns (single-crystal X-ray diffraction data). The XRD patterns of the solid solutions $Cu_2Mn_{1-x}Co_xSnS_4$ (x=0.2; 0.4; 0.6 and 0.8) were fully indexed in the space group $I\bar{4}$ (no. 82), and the observed interlayer spacing showed a good agreement with those calculated from the crystal structure. As expected, it is found an

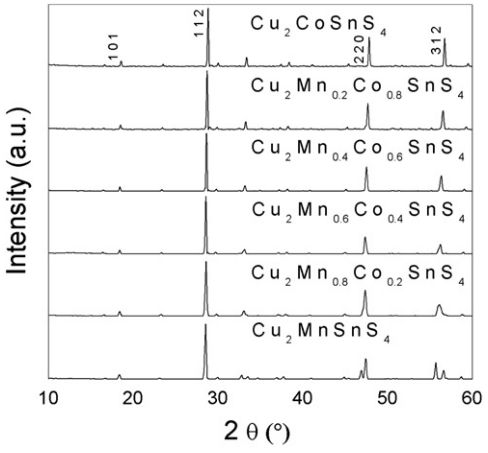

Fig. 3. X-ray powder diffraction patterns obtained for $Cu_2Mn_{1-x}Co_xSnS_4$ (x=0, 0.2, 0.4, 0.6, 0.8 and 1.0).

Table 6
Chemical composition analysis (% mass) of $Cu_2Mn_{1-x}Co_xSnS_4$ and end-members.

Cu	Mn	Co	Sn	S	Estimated	Nominal
30.7	0	12.1	27.9	29.2	$Cu_{2.35}Co_{1.00}Sn_{1.15}S_{4.44}$	Cu_2CoSnS_4
29.3	2.6	10.8	27.1	29.5	$Cu_{1.96}Mn_{0.20}Co_{0.78}Sn_{1.00}S_{3.91}$	$Cu_2Mn_{0.2}Co_{0.8}SnS_4$
30.0	5.2	8.1	27.0	29.7	$Cu_{2.08}Mn_{0.42}Co_{0.60}Sn_{1.00}S_{4.08}$	$Cu_2Mn_{0.4}Co_{0.6}SnS_4$
29.4	8.2	4.8	27.6	29.7	$Cu_{1.99}Mn_{0.64}Co_{0.35}Sn_{1.00}S_{3.97}$	$Cu_2Mn_{0.6}Co_{0.4}SnS_4$
29.9	9.5	3.6	27.1	29.9	$Cu_{2.07}Mn_{0.76}Co_{0.28}Sn_{1.00}S_{4.09}$	$Cu_2Mn_{0.8}Co_{0.2}SnS_4$
30.2	13.5	0	26.8	29.5	$Cu_{2.10}Mn_{1.09}Sn_{1.00}S_{4.07}$	Cu_2MnSnS_4

Table 7
Cell parameters data for $Cu_2Mn_{1-x}Co_xSnS_4$ (space group $I\bar{4}$) and end-members (space group $I\bar{4}2m$).

Phase	*a* (Å)	*c* (Å)	Cell volume
Cu_2CoSnS_4	5.395(±0.008)	10.789(±0.003)	314.1
$Cu_2Mn_{0.2}Co_{0.8}SnS_4$	5.415(±0.002)	10.823(±0.001)	317.3
$Cu_2Mn_{0.4}Co_{0.6}SnS_4$	5.434(±0.003)	10.856(±0.001)	320.6
$Cu_2Mn_{0.6}Co_{0.4}SnS_4$	5.442(±0.009)	10.888(±0.006)	322.4
$Cu_2Mn_{0.8}Co_{0.2}SnS_4$	5.446(±0.004)	10.888(±0.002)	322.9
Cu_2MnSnS_4[a]	5.548(±0.001)	10.844(±0.002)	333.78

[a] Ref. [30].

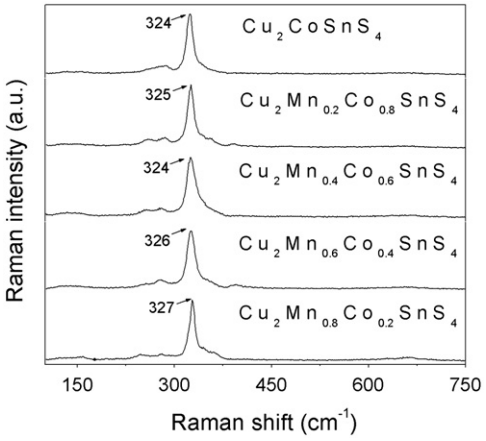

Fig. 4. Raman spectra of solid solutions and Cu_2CoSnS_4 end-member.

expansion of the cell due to the substitution of Co^{2+} by a larger cation Mn^{2+}. The values of the cell parameters for all phases are given in Table 7. We propose a continuous solid solution on the basis of the cell parameter trends determined by X-ray powder diffraction. The Raman spectra of powder samples at room temperature are shown in Fig. 4. The spectra are characterized by one strong line at approximately 330 cm^{-1}, which is consistent with the presence of the SnS_4 unit by analogy to Raman spectra of Cu_2MSnS_4 compounds (M=Mn, Fe, Zn,Cd, Hg) [33,34].

3.3. Magnetic susceptibility

The zero-field-cooled (ZFC)/field-cooled (FC) magnetization cycle, performed under low magnetic fields (500 Oe), is shown in Fig. 5 for the $Cu_2Mn_{0.6}Co_{0.4}SnS_4$ phase. It can be seen that the zero-field-cooled magnetization M^{ZFC} first increases with increasing temperature, reaches a maximum at T_N=7.7 K (Néel temperature) and then decreases steadily down to the paramagnetic regime. Such behavior is characteristic of antiferromagnetic interactions, in agreement with reported results for Cu_2MnSnS_4 [35]. Fig. 5 shows a narrow peak of the susceptibility at T_N and a very weak irreversibility of the ZFC/FC cycle at $T<T_N$. One possible explanation to such irreversibility comes from the fact that, due to the statistical occupation of the tetrahedral site by Mn and Co, observable contributions of two different sublattices coexist in the system, in such a way that a slight ferromagnetic component is generated through the canting of the overall moment. The paramagnetic regime was analyzed well above the magnetic transition temperature, under high applied fields (10 kOe). The inverse susceptibility, $1/\chi$, was fitted by a classical Curie–Weiss relation $\chi=C/(T-\theta)$, in the range 150 K ≤ T ≤ 400 K (inset, Fig. 5), from which the effective moment μ_{eff} and the Curie–Weiss temperature θ were obtained. The observed effective

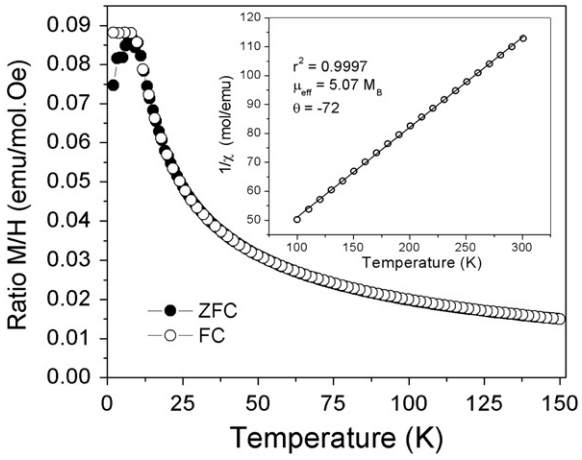

Fig. 5. Zero-field-cooled/field-cooled magnetization cycles at 500 Oe (ZFC: filled symbols; FC: open symbols) for $Cu_2Mn_{0.6}Co_{0.4}SnS_4$. The *inset* shows the $1/\chi$-*versus*-temperature plot fitted by a Curie–Weiss law.

moment of $Cu_2Mn_{0.6}Co_{0.4}SnS_4$ (μ_{eff}=5.07μ_B) is quite close to the expected moment for a nominal cationic composition of 0.6 Mn^{2+} and 0.4 Co^{2+} (5.2μ_B). In addition, the negative value of the Curie–Weiss temperature (θ=−72 K), indicates the existence of strong antiferromagnetic interactions.

4. Conclusions

New stable solid solutions of $Cu_2Mn_{1-x}Co_xSnS_4$ (x=0.2, 0.4, 0.6 and 0.8) compounds were obtained by conventional solid-state synthesis method. The characterization of the materials by Raman spectroscopy and powder X-ray diffraction indicates that all phases have similar crystal structures and crystallize in the tetragonal system. The magnetic susceptibility measurements show an antiferromagnetic behavior. The crystal structure obtained by single crystal X-ray diffraction of the $Cu_2Mn_{0.2}Co_{0.8}SnS_4$ and $Cu_2Mn_{0.4}Co_{0.6}SnS_4$ phases corresponds to the këwhile-type structure, both phases being isostructural. In both phases, the closest to an ideal tetrahedra are the SnS_4 units and those with larger distortion are the $Cu(2)S_4$ motifs. The average distortion (% EDL) of the tetrahedra in both phases is approximately 1%. The average volumes of $Cu_2Mn_{0.2}Co_{0.8}SnS_4$ (4.4%) and $Cu_2Mn_{0.4}Co_{0.6}SnS_4$ (3.6%), calculated with the Pfitzner model show a significant difference with the limit Cu_2MnSnS_4 phase (6.0%) of structural stannite-type. In our knowledge, the solid solutions of the $Cu_2Mn_{1-x}Co_xSnS_4$ type are the first with këwhile-type lattice reported in literature.

Supporting material

The crystallographic data for $Cu_2Mn_{0.2}Co_{0.8}SnS_4$ and $Cu_2Mn_{0.4}Co_{0.6}SnS_4$ have been deposited with FIZ Karlsruhe as CSD-number 424674 and 424675. These data may be obtained free of charge by contacting FIZ Karlsruhe at +497247808666 (fax) or crysdata@fiz-karlsruhe.de (e-mail).

Acknowledgments

The authors thank to Vincent Dorcet (CDFIX of the Université de Rennes 1, France) for the X-ray intensity data collections. Beca de Apoyo Tesis Doctoral AT-24100053 and ECOS-CONICYT C09-E01. Authors belong to the French-Chilean CNRS international Joint laboratory LIA-MIF no. 816.

References

[1] B.R. Pamplin, J. Phys. Chem. Solids 25 (1964) 675–684.
[2] L. Guen, W.S. Glaunsinger, J. Solid State Chem. 21 (1980) 10–21.
[3] K.E. Newman, X. Xiang, Phys. Rev. B Rapid Commun. 44 (1991) 4677–4680.
[4] S. Chen, A. Walsh, Y. Luo, J.-H. Yang, X. Gong, S.-H. Wei, Phys. Rev. B 82 (2010) 195203.
[5] R. Osorio, Z.W. Lu, S.-H. Wei, A. Zunger, Phys. Rev. B 47 (1993) 9985–9988.
[6] S. Schorr, V. Riede, D. Spemann, T. Doering, J. Alloys Compd. 414 (2006) 26–30.
[7] S. Chen, X. Gong, A. Walsh, S.-H. Wei, Phys. Rev. B 79 (2009) 165211.
[8] S. Siebentritt, Thin Solid Films 403–404 (2002) 1–8.
[9] B.A. Andersson, Prog. Photovoltaics: Res. Appl. 8 (2000) 61–76.
[10] H. Katagiri, Thin Solid Films 480–481 (2005) 426–432.
[11] R. Schurr, A. Hölzing, S. Jost, R. Hock, T. Voβ, J. Schulze, A. Kirbs, A. Ennaoui, M. Lux-Steiner, A. Weber, I. Kötschau, H.-W. Schock, Thin Solid Films 517 (2009) 2465–2468.
[12] D.M. Schleich, A. Wold, Mater. Res. Bull. 12 (1977) 111–114.
[13] S.R. Hall, J.T. Szymansk, J.M. Stewart, Can. Mineral. 16 (1978) 131–137.
[14] P. Bonazzi, L. Bindi, G.P. Bernardini, S. Menchetti, Can. Mineral. 41 (2003) 639–647.
[15] S. Schorr, H.A.-J.O. Hoebler, M.I. Tovar, Eur. J. Mineral. 19 (2007) 65–73.
[16] S. Schorr, Thin Solid Films 515 (2007) 5985–5991.
[17] T. Bernert, A. Pfitzner, Z. Kristallogr. 220 (2005) 968–972.
[18] L.D. Gulay, O.P. Nazarchuk, I.D. Olekseyuk, J. Alloys Compd. 377 (2004) 306–311.
[19] U.1997–2004 COLLECT, Software for CCD diffractometers, Bruker AXS Inc., Madison, WI, n.d.
[20] A.J.M. Duisenberg, A.M.M. Schreurs, J. Appl. Crystallogr. 36 (2003) 220.
[21] A.J.M. Duisenberg, R.W.W. Hooft, A.M.M. Schreurs, J. Kroon, J. Appl. Crystallogr. 33 (2000) 893.
[22] U. SMART, SAINTPLUS V6.02, SHELXTL V6.10; Bruker Analytical X-ray Instrument Inc., Madison, WI, n.d.
[23] U.1996 SADABS, Area-Detector Absorption Correction, Siemens Industrial Automation Inc., Madison, WI, n.d.
[24] G.M. Sheldrick, SHELXL-97 Program for Solution and Refinement of Crystal Structures, University of Göttingen, 1997.
[25] K. Brandenburg, DIAMOND, Visual Crystal Structure Information System, Version 2.1e Crystal Impact GbR, Bonn, Germany, 1999.
[26] A.L. Spek, J. Appl. Crystallogr. 36 (2003) 7–13.
[27] P. for the I. of X. experiments CHECKCELL, J. Laugier, B. Bochu, Laboratoire Des Matériaux Et Du Génie Physique Ecole Nationale Supérieure De Physique De Grenoble (INPG) Domaine Universitaire BP 46, 38402 Saint Martin d'Hères France, http://www.inpg.fr/LMGP (n.d.).
[28] T. Bernert, M. Zabel, A. Pfitzner, J. Solid State Chem. 179 (2006) 849–854.
[29] T. Bernert, A. Pfitzner, Z. Anorg. Allg. Chem. 632 (2006) 1213–1218.
[30] K. Robinson, G.V. Gibbs, P.H. Ribbe, Science 172 (1971) 567–570.
[31] R.D. Shannon, Acta Crystallogr. A 32 (1976) 751–767.
[32] T. Bernert, Untersuchungen Zum Einfluss Der Tetraedervolumina Auf Den Strukturtyp in Quaternären Zinkblende- Und Wurtzitvarianten Dissertation, Universität Regensburg, 2005.
[33] M. Himmrich, H. Haeuseler, Spectrochim. Acta Part A: Mol. Spectrosc. 47 (1991) 933–942.
[34] P.A. Fernandes, P.M.P. Salomé, A.F. Cunha, J.Alloys Compd. 509 (2011) 7600–7606.
[35] T. Fries, Y. Shapira, F. Palacio, M.C. Moro, G.J. Mcintyre, R. Kershaw, A. Wold, E.J. McNiff Jr., Phys. Rev. B 56 (1997) 5424–5431.